JM PAPERS

Non-axisymmetric patterns in floating viscoplastic films

Thomasina V. Ball[1] **and Neil J. Balmforth**[2]

[1]Mathematics Institute, University of Warwick, Coventry CV4 7AL, UK
[2]Department of Mathematics, University of British Columbia, Vancouver, BC V6T 1Z2, Canada
Corresponding author: Thomasina V. Ball, thomasina.ball@warwick.ac.uk

Experiments are presented to explore the non-axisymmetric instabilities of spreading films of aqueous suspensions of Carbopol and Xanthan gum floating on a bath of perfluoropolyether oil. The experimental observations are compared against theoretical predictions exploiting a shallow-film model in which the viscoplastic rheology is captured by the Herschel–Bulkley constitutive law. With this model, we construct axisymmetric base states that evolve from the moment that the film floats onto the bath, out towards long times at which spreading becomes self-similar, and then test their linear stability towards non-axisymmetric perturbations. In the geometry of a thinning expanding film, we find that shear thinning does not drive a loss of axisymmetry at early times (when the degree of expansion is small), but when the film has expanded in radius by a factor of two or so, shear-thinning hoop stresses drive non-axisymmetric instabilities. Unstable modes possess relatively low angular wavenumber, and the loss of symmetry is not particularly dramatic. When the oil in the bath is replaced by salty water, the experiments are completely different, with dramatic non-axisymmetric patterns emerging from interfacial effects.

1. Introduction

Floating films of complex fluid feature in several problems in the geosciences and engineering. When such films float atop a much less viscous Newtonian fluid, the spreading flow experiences little bottom drag and the extensional stresses in the film control flow. For a thin viscous film, one can then compactly capture the dynamics within a reduced model (Oron *et al.* 1997; Craster & Matar 2009), as used in explorations of the spreading of oil films over water (di Pietro & Cox 1979; Koch & Koch 1995).
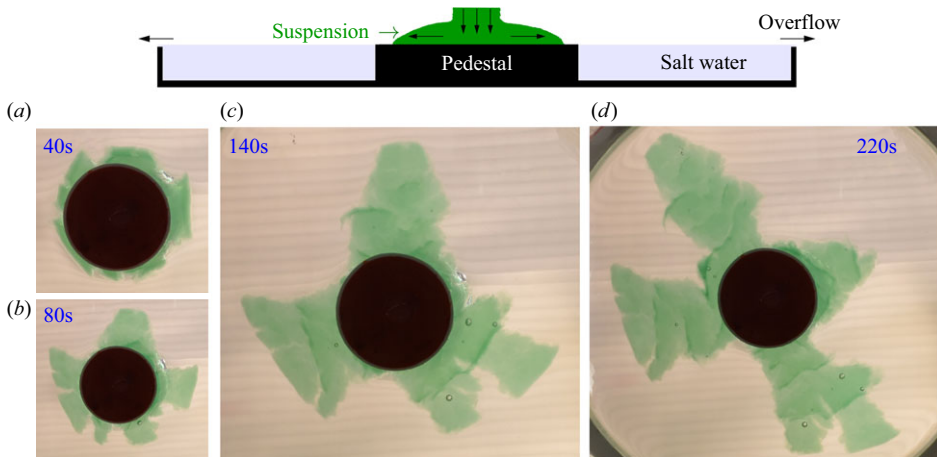
Figure 1. An experiment in which a suspension of Xanthan gum (dyed green; density 1g/cm^3) spreads out over a bath of water made denser by salt (NaCl, to a density of 1.15g/cm^3; colourless). The dark circle at the centre shows the position of a pedestal, the top surface of which is above the oil surface and onto which the Xanthan gum is poured, to create a localized source. The pedestal has a radius of $\mathcal{L} = 1.7$cm, and the times of the photographs (taken from above) after the Xanthan gum enters the oil are indicated. The container for the bath is completely filled, so that any depth changes are prevented by overflow.

Generalizations of such models to power-law fluids have been exploited to study the dynamics of ice shelves (MacAyeal & Barcilon 1988; MacAyeal 1989; Schoof & Hewitt 2013) and the Earth's crust (England & McKenzie 1982, 1983).

Although floating viscous films spread out axisymmetrically from localized sources (Pegler & Worster 2012), it has been observed that aqueous suspensions of Xanthan gum do not. Instead, such non-Newtonian films suffer a dramatic non-axisymmetric instability (Sayag & Worster 2019a), at least when floated out above a layer of salty water. An illustration of this type of pattern formation is displayed in figure 1. In this experiment, an aqueous suspension of Xanthan gum is floated out onto a bath of salt solution. The moment that the Xanthan gum enters the bath, axisymmetry is immediately lost (the gum spreads axisymmetrically over a pedestal that acts as the localized source).

In order to rationalize such observations, Sayag & Worster (2019b) analysed the inertialess linear stability of an expanding cylinder of power-law fluid. They confirmed the presence of non-axisymmetric linear instability, driven by non-Newtonian hoop stresses acting at the advancing fluid edge. Although these instabilities arise mostly at early times and are relatively weak (Ball *et al.* 2021), Ball & Balmforth (2021) demonstrated that the instability carried over to radially spreading films and was potentially stronger if the fluid film also possessed a yield stress. For the task, Ball & Balmforth (2021) exploited a thin-film model for a viscoplastic fluid described by the Herschel–Bulkley constitutive law (Balmforth *et al.* 2014).

In the present paper, we revisit the experiments conducted by Sayag & Worster (2019a) in order to examine the effect of the fluid filling the bath underneath the floating film. The experiments by Sayag & Worster, and those shown in figure 1, employ salty water for the bath, but water is also the solvent used for the Xanthan gum. In this regard, Ball *et al.* (2022) noted that aqueous suspensions of Carbopol gel (a complex fluid with shear-thinning viscosity and a yield stress) spreading over wetted planes suffered dramatic non-axisymmetric instabilities taking the form of fracture-like patterns. These patterns owed their presence to the thin pre-wetted layer of water: when the plane was dry, or when

it was wetted by a thin layer of immiscible fluid, the patterns did not appear. Instead, the viscoplastic fluid expanded axisymmetrically in the usual manner of a gravity current (with vertical shear stresses dominating the resistance to spreading). Ball & Balmforth (2021) suggested that the patterns therefore arose not from a non-axisymmetric hydrodynamic instability, but from solid-like fracture, exacerbated by the presence of the pre-wetted water film that reduced the fracture toughness on contact. Similar patterns and phenomena arise in viscoplastic displacement flows through Hele-Shaw cells (Ball *et al.* 2021; Hutchinson & Worster 2024).

To eliminate the possibility that effects of this sort impact the Sayag & Worster experiment, one must therefore avoid using a water-based fluid for the bath. In the experiments conducted here, we instead employ a perfluoropolyether oil, which is significantly denser than water and immiscible, permitting an exploration of the Sayag–Worster instability for a spreading, floating film. We also use aqueous suspensions of Carbopol in addition to Xanthan gum, to test whether a notable yield stress can prompt stronger instability.

To complement these experiments, we provide theoretical predictions based on the thin-film model developed by Ball & Balmforth (2021). In this model, axisymmetric base states are constructed that evolve from the moment that the film floats onto the bath, out towards long times at which spreading becomes self-similar. The linear stability of these states is then explored by solving an initial-value problem for non-axisymmetric perturbations, spanning the early- and late-time dynamics. One difference with our earlier analysis is that we use here a different inner radial boundary condition that is more suitable to the experiments: those tests are conducted by placing a pedestal in the bath whose surface protrudes above the oil surface. The viscoplastic fluid is emplaced on this pedestal from above, spreading axisymmetrically before the film is launched into the bath (see figure 1). Above the pedestal, however, the film becomes substantially deeper because the fluid does not slide freely over its top. The abrupt thinning of the film on detachment from the pedestal demands a boundary condition that we derive in § 2, where we summarize the theoretical model more completely. In this section, we further use the model to build axisymmetric spreading states and test their linear stability towards non-axisymmetric perturbations. Section 3 outlines our experiments, their analysis and the comparison with the theoretical results.

2. Shallow-film model

Figure 2 presents a sketch of the geometry used for the theoretical model, in addition to a photograph of the set-up used for the experiments. Cylindrical polar coordinates describe the geometry of the model, which describes the expansion of a thin, floating film of a Herschel–Bulkley fluid. The flow over the pedestal is not captured by the model, but replaced by suitable boundary conditions at the edge of the pedestal, which has radius $\mathcal{L}$. Similarly, in the usual manner of a thin-film analysis in which sharp horizontal adjustments cannot be captured, the viscoplastic fluid is assumed to instantaneously descend to its level of neutral buoyancy on entry to the bath, resulting in a film profile like that illustrated in figure 2.

When the bath is sufficiently deep or its viscosity is sufficiently small, the drag on the floating film is not sufficient to generate significant vertical shear. The flow then becomes plug-like throughout its depth, with horizontal velocity components, $u \sim u(r, \vartheta, t)$ and $v \sim v(r, \vartheta, t)$. Providing the characteristic film thickness $\mathcal{H}$ remains much less than $\mathcal{L}$, the stage is then set for a standard type of free thin-film analysis, for which a reduced model follows by integrating the governing fluid equations over the film's depth
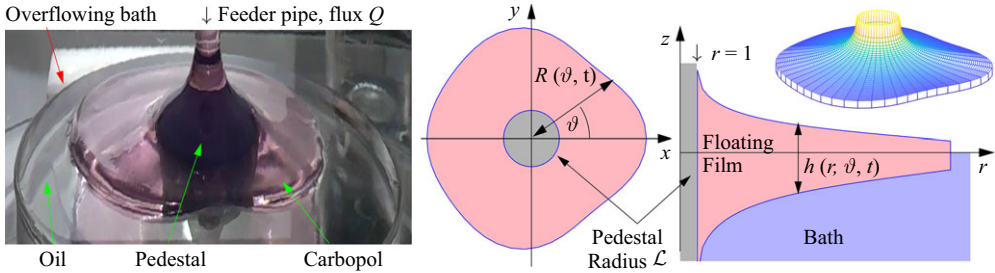
Figure 2. Photograph of the experiment (left) and sketches of the film geometry (right), showing a view from above, a vertical cross-section and an inclined perspective. In the model, we assume that the fluid instantaneously adjusts to its level of neutral buoyancy once it flows off the pedestal, which has radius $\mathcal{L}$. After scaling horizontal lengths by $\mathcal{L}$, the domain of the dimensional model consists of radii $r \geq 1$; the influx of fluid from the pedestal (shaded grey) is treated by imposing suitable boundary conditions at $r = 1$.

(Oron *et al.* 1997; MacAyeal & Barcilon 1988; MacAyeal 1989; Balmforth 2018). This exercise was established in the present context of a viscoplastic film by Ball & Balmforth (2021), although they considered fluid sliding freely over a flat surface. Here, instead, we consider a partly submerged, floating film. Nevertheless, it is straighforward to incorporate this submergence by simply taking the depth of the current above the top of the bath to be a fraction $(\rho_b - \rho)/\rho_b$ of the total film depth, where ρ is the film density and ρ_b that of the bath (e.g. MacAyeal & Barcilon (1988)). For the fluids used in our experiments (see table 1), approximately half of the film is submerged. Moreover, we further account for the effect of buoyancy by introducing the reduced gravity $g' \equiv g(\rho_b - \rho)/\rho_b$, where g denotes gravitational acceleration.

Although the model does not account for the flow over the pedestal in detail, one aspect of that flow does impact the formulation: when the viscoplastic fluid flows onto the pedestal from the feeder pipe, it forms a gravity current that spreads relatively slowly in comparison with the expansion of the floating film. As the film descends off the pedestal, the fluid therefore thins dramatically, much like the flow around the grounding line between an ice sheet and shelf (e.g. Schoof (2007, 2011); Schoof & Hewitt (2013)). In the thin-film model, this implies that the starting depth of the floating film should be relatively large, but the horizontal velocity should be corresponding small, so that the dimensional radial volume flux is kept at constant value Q. In principle, one should consider the full, Stokes-like problem here, in view of a lack of any separation in the vertical and horizontal scales. We avoid any such match here, however, and formulate effective boundary conditions at the inner edge of the floating film that take some account of the significant thickening that takes place there.

2.1. *Scaling*

In the reduction of the governing equations performed by Ball & Balmforth (2021), the dimensions are removed from the problem by scaling vertical and radial distances by the characteristic scales $\mathcal{H}$ and $\mathcal{L}$, respectively. The horizontal velocity components u and v are scaled by $\mathcal{V} = Q/(\mathcal{H}\mathcal{L})$, and the vertical velocity w by $\mathcal{H}\mathcal{V}/\mathcal{L}$, where Q is the volume flux. Time is scaled by $\mathcal{T} = \mathcal{L}/\mathcal{V}$. The stresses and pressure are scaled by the hydrostatic scale $\rho g' \mathcal{H}$.

The Herschel–Bulkley law has three parameters: the yield stress τ_Y, the power-law index n and the consistency K. This constitutive law relates the (dimensional) second invariants of the stress, τ, and deformation-rate tensor, $\dot{\gamma}$, through $\tau = \tau_Y + K\dot{\gamma}^n$ (Balmforth *et al.*

		Carbopol	Xanthan gum
Bath viscosity (at 25°C)	μ_b	26 mPa s	
Bath density	ρ_b	1.85 g cm^{-3}	
Bath depth	$\mathcal{H}_b$	10.5 − 18 mm	
Pedestal radius	$\mathcal{L}$	1.7 cm	
		Carbopol	Xanthan gum
Yield stress	τ_Y	20 Pa	−
Consistency	K	10 Pa s^n	32 Pa s^n
Power-law index	n	0.4	0.12
Density	ρ	1 g cm^{-3}	1 g cm^{-3}
Surface tension (water–air)	γ_{wa}	72 mN m^{-1}	72 mN m^{-1}
Surface tension (water–oil)	γ_{wo}	$\sim 20 - 40$ mN m^{-1}	$\sim 20 - 40$ mN m^{-1}
Volume flux	Q	1.25 − 160 ml min^{-1}	2.5 − 20 ml min^{-1}
Height scale	$\mathcal{H} = (KQ^n/\rho g' \mathcal{L}^{2n})^{\frac{1}{n+1}}$	0.8 − 3.3 mm	4.7 − 5.8 mm
Time scale	$\mathcal{T} = (K\mathcal{L}^2/\rho g' Q)^{\frac{1}{n+1}}$	0.4 − 11.6 s	5.1 − 32.4 s
Bingham number	$Bi = \tau_Y (\mathcal{L}^2/\rho g' K^{\frac{1}{n}} Q)^{\frac{n}{n+1}}$	1.3 − 5.3	−
Shear stress of bath vs film	Equation (2.4)	$(1-4) \times 10^{-2}$	$(1-9) \times 10^{-4}$
Capillary length (water–air)	$\lambda_{c,wa} = (\gamma_{wa}/\rho g)^{1/2}$	2.7 mm	2.7 mm
Capillary length (water–oil)	$\lambda_{c,wo} = (\gamma_{wo}/(\rho_b - \rho)g)^{1/2}$	$\sim 1.5 - 2.2$ mm	$\sim 1.5 - 2.2$ mm

Table 1. Experimental parameters, scales and dimensionless groupings. For the interfacial tensions quoted (γ_{wa}, γ_{wo}), we assume that the Carbopol and Xanthan gum solutions are similar to water, and the perfluorinated oil similar to other oils, and use typical values quoted in the literature.

2014). The consistency K and characteristic strain rate, $\mathcal{V}/\mathcal{L}$, can be combined into a stress scale $K(\mathcal{V}/\mathcal{L})^n$ which, when balanced with $\rho g'\mathcal{H}$ provides the vertical length scale

$$\mathcal{H} = \left(\frac{KQ^n}{\rho g' \mathcal{L}^{2n}} \right)^{\frac{1}{n+1}}. \tag{2.1}$$

Hence

$$\mathcal{T} = \frac{\mathcal{H}\mathcal{L}^2}{Q} = \left(\frac{K\mathcal{L}^2}{\rho g' Q} \right)^{\frac{1}{n+1}}. \tag{2.2}$$

Two parameters remain from the scaling of the Herschel–Bulkley law: the power-law index n and a Bingham number related to the dimensional yield stress τ_Y

$$Bi = \frac{\tau_Y \mathcal{H}^n \mathcal{L}^{2n}}{KQ^n} = \tau_Y \left(\frac{\mathcal{L}^2}{\rho g' K^{\frac{1}{n}} Q} \right)^{\frac{n}{n+1}}. \tag{2.3}$$

The parameters n and Bi feature in our model solutions; we exploit the time scale $\mathcal{T}$ in our interrogation of experimental results.

The scales above can be used to gauge the importance of physical effects that are not incorporated into the model. For example, to estimate the importance of viscous drag from the bath, we note that, although the bath is deep relative to the film thickness, it remains shallower than $\mathcal{L}$. The main drag therefore stems from vertical shear stresses, of order $\mu_b \mathcal{V}/\mathcal{H}_b$, if μ_b and $\mathcal{H}_b$ are the viscosity and depth of the bath. The vertical shear stress in the film, on the other hand, is $O(\rho g' \mathcal{H}^2/\mathcal{L})$. The importance of drag can therefore be

measured by the ratio

$$\frac{\mu_b \mathcal{V} \mathcal{L}}{\rho g' \mathcal{H}^2 \mathcal{H}_b} \equiv \frac{\mu_b}{\mathcal{H}_b} \left[\frac{(\rho g')^{2-n} Q^{1-2n} \mathcal{L}^{6n}}{K^3} \right]^{\frac{1}{n+1}}. \tag{2.4}$$

Estimates based on our experiments in § 3 (table 1) indicate that this ratio is $O(10^{-4}) - O(10^{-2})$. Hence, drag from the bath is not significant. That said, once the film spreads sufficiently far from the launch stage, the radius of the pedestal is not necessarily the best choice for the horizontal length scale $\mathcal{L}$. Nevertheless, we observed no significant differences in the dynamics when a subset of the experiments were repeated with a bath of almost twice the depth. The omission of surface tension is a little more tricky to justify, an issue we return to later.

2.2. *Model equations*

In the polar coordinates (r, ϑ), the dimensionless mathematical model combines the depth-integrated conservation of mass and momentum equations for the fluid depth $h(r, \vartheta, t)$ and horizontal velocity (u, v), with the leading-order Herschel–Bulkley constitutive law relating the horizontal stresses $\{\tau_{rr}, \tau_{r\theta}, \tau_{\theta\theta}\}$ and strain rates $\{\dot{\gamma}_{rr}, \dot{\gamma}_{\theta\theta}, \dot{\gamma}_{r\theta}\}$. The model equations are

$$\frac{\partial h}{\partial t} + \frac{1}{r}\frac{\partial}{\partial r}(rhu) + \frac{1}{r}\frac{\partial}{\partial \vartheta}(vh) = 0, \tag{2.5}$$

$$\frac{\partial}{\partial r}\left[\frac{1}{2}h^2 - h(2\tau_{rr} + \tau_{\theta\theta})\right] - \frac{1}{r}\frac{\partial}{\partial \vartheta}(h\tau_{r\theta}) + \frac{h}{r}(\tau_{\theta\theta} - \tau_{rr}) = 0, \tag{2.6}$$

$$\frac{1}{r}\frac{\partial}{\partial \vartheta}\left[\frac{1}{2}h^2 - h(2\tau_{\theta\theta} + \tau_{rr})\right] - \frac{\partial}{\partial r}(h\tau_{r\theta}) - \frac{2}{r}h\tau_{r\theta} = 0. \tag{2.7}$$

$$\begin{cases} \dot{\gamma} = 0, & \tau < Bi, \\ [\tau_{rr}, \tau_{\theta\theta}, \tau_{r\theta}] = \left(\dfrac{Bi}{\dot{\gamma}} + \dot{\gamma}^{n-1}\right)[\dot{\gamma}_{rr}, \dot{\gamma}_{\theta\theta}, \dot{\gamma}_{r\theta}], & \tau \geq Bi, \end{cases} \tag{2.8}$$

with

$$[\dot{\gamma}_{rr}, \dot{\gamma}_{\theta\theta}, \dot{\gamma}_{r\theta}] = \left[2\frac{\partial u}{\partial r}, \frac{2}{r}\left(u + \frac{\partial v}{\partial \vartheta}\right), \frac{1}{r}\left(\frac{\partial u}{\partial \vartheta} - v\right) + \frac{\partial v}{\partial r}\right], \tag{2.9}$$

where $\dot{\gamma} = \sqrt{\dot{\gamma}_{rr}^2 + \dot{\gamma}_{r\theta}^2 + \dot{\gamma}_{\theta\theta}^2 + \dot{\gamma}_{rr}\dot{\gamma}_{\theta\theta}}$ and $\tau = \sqrt{\tau_{rr}^2 + \tau_{r\theta}^2 + \tau_{\theta\theta}^2 + \tau_{rr}\tau_{\theta\theta}}$.

At the outer edge, $r = R(\vartheta, t)$, we impose the kinematic condition, and demand that the net normal and tangential stresses vanish

$$\frac{\partial R}{\partial t} + \frac{v}{R}\frac{\partial R}{\partial \vartheta} = u, \tag{2.10}$$

$$\frac{1}{2}h^2 - h\left[\tau_{rr} + \tau_{\theta\theta} + \frac{R}{\sqrt{R^2 + R_\vartheta^2}}\left(\tau_{rr} - 2\frac{R_\vartheta}{R}\tau_{r\theta} + \frac{R_\vartheta^2}{R^2}\tau_{\theta\theta}\right)\right] = 0, \tag{2.11}$$

$$\tau_{r\theta} - \frac{R_\vartheta}{R}(\tau_{\theta\theta} - \tau_{rr}) - \frac{R_\vartheta^2}{R^2}\tau_{r\theta} = 0. \tag{2.12}$$

Here and below we use the subscripts (r, ϑ) to denote partial derivatives, which can be distinguished by typeface from our notation (r, θ) for the tensor components.

We position the inner edge of the film slightly beyond the radius of the pedestal, at $r = 1 + \varepsilon$ with $\varepsilon \ll 1$. Here, we impose the incoming flux and angular velocity

$$2\pi h u = 1, \quad v = 0. \tag{2.13}$$

The abrupt increase in film thickness, implied by the match to the incoming gravity current over the pedestal, can be imposed by taking $h(1 + \varepsilon, t)$ to diverge suitably for $\varepsilon \to 0$, as we explain below.

2.3. *Axisymmetric spreading solutions*

From (2.6)–(2.8), axisymmetric spreading states, with

$$h = H(r, t), \ u = U(r, t), \ v = 0, \ R = \overline{R}(t), \ [\tau_{\mathrm{rr}}, \tau_{\mathrm{r}\theta}, \tau_{\theta\theta}] = [T_{\mathrm{rr}}(r, t), 0, T_{\theta\theta}(r, t)],$$

satisfy the equations

$$H_t + \frac{1}{r}(rHU)_r = 0, \tag{2.14}$$

$$\left[\frac{1}{2}H^2 - H(2T_{\mathrm{rr}} + T_{\theta\theta})\right]_r + \frac{H}{r}(T_{\theta\theta} - T_{\mathrm{rr}}) = 0, \tag{2.15}$$

$$[T_{\mathrm{rr}}, T_{\theta\theta}] = \left(\frac{Bi}{\dot{\Gamma}} + \dot{\Gamma}^{n-1}\right)\left[2U_r, \frac{2U}{r}\right], \qquad \dot{\Gamma} = 2\sqrt{U_r^2 + \frac{1}{r}UU_r + \frac{1}{r^2}U^2}, \tag{2.16}$$

along with the boundary conditions

$$\left[\frac{1}{2}H^2 - H(2T_{\mathrm{rr}} + T_{\theta\theta})\right]_{r=\overline{R}} = 0, \quad 2\pi HU|_{r\to 1} = 1, \tag{2.17}$$

and

$$\overline{R}_t = U(\overline{R}, t), \tag{2.18}$$

extending the shorthand subscript notation for partial derivatives to t.

Very close to the pedestal when $r - 1 = O(\varepsilon) \ll 1$, the radial derivatives become $O(\varepsilon^{-1})$. The main balances in (2.14)–(2.16) are then

$$(HU)_r \sim 0, \quad \left(H^2/2 - 2HT_{\mathrm{rr}}\right)_r \sim 0, \quad T_{\mathrm{rr}} \sim 2^n |U_r|^n \mathrm{sgn}(U_r) \gg T_{\theta\theta}, \tag{2.19}$$

implying that the dynamics is controlled by the radial, power-law viscous stress. Hence,

$$H \sim \frac{1}{2\pi U} \quad \text{and} \quad T_{\mathrm{rr}} \sim \frac{1}{4}H \sim \frac{1}{8\pi U}, \tag{2.20}$$

given that T_{rr} must decline to $O(1)$ values further from the pedestal. Consequently,

$$U \sim \left[\frac{(1+n)^n}{8\pi(2n)^n}(r-1)^n\right]^{\frac{1}{n+1}} \quad \text{and} \quad H \sim 4\left[4\pi\frac{(1+n)}{n}(r-1)\right]^{-\frac{n}{n+1}}. \tag{2.21}$$

For early times, the kinematic condition in (2.17) also implies that

$$\overline{R} \sim 1 + \frac{t^{n+1}}{8\pi(2n)^n(n+1)}. \tag{2.22}$$

We translate the preceding results into effective boundary and initial conditions as follows: instead of dealing with diverging conditions for $r \to 1$, we instead place the

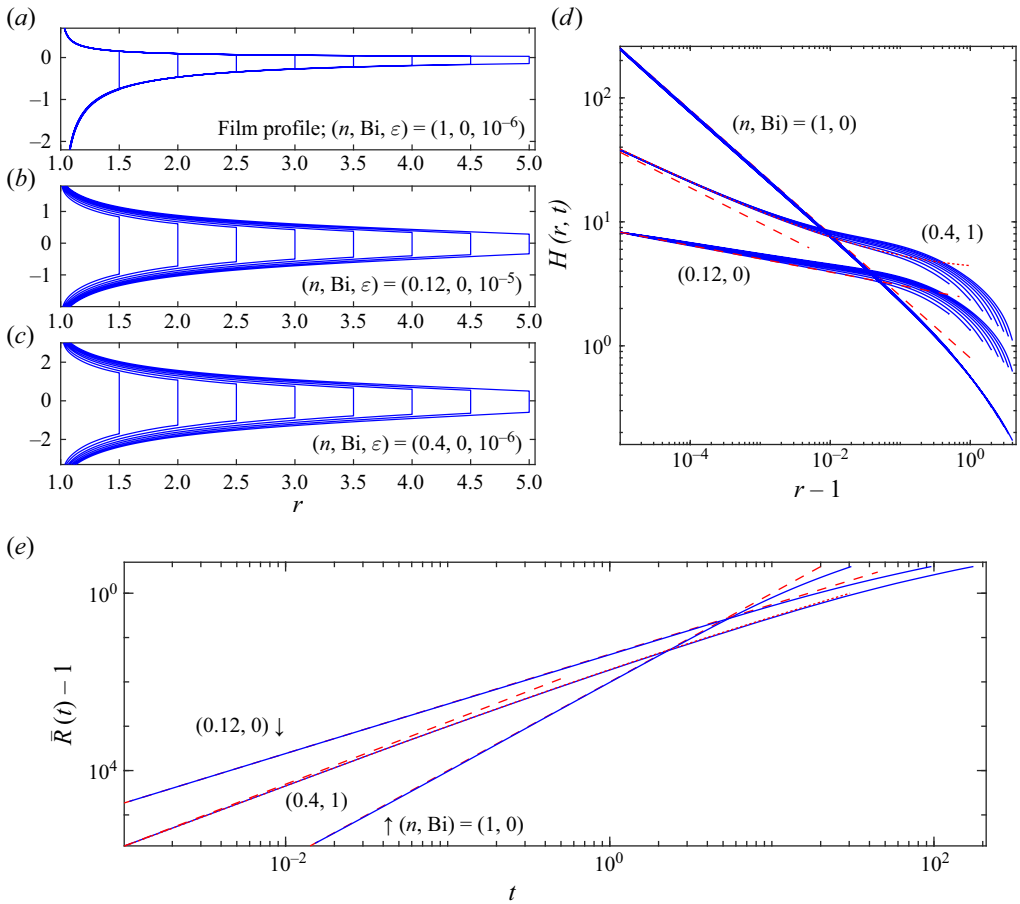Figure 3. (*a,b,c*) Axisymmetric solutions for the values of (n, Bi, ε) indicated. Shown are film profiles at equivalent outer radii, for baths with density ratios 0.83 (panel (*a*)) and $\rho/\rho_b = 0.54$ (panels (*b,c*)). The profiles of $H(r, t)$ are replotted on a loglog scale in (*d*) and compared with (2.21) (red dashed lines). Panel (*e*) shows time series of the outer radius $\overline{R}(t)$ for the three solutions, with the (red) dashed lines showing (2.22). In (*d*) and (*e*) the modified early time solution (2.23) for $Bi = 1$ is shown by the (red) dotted lines.

inner edge of the computation at $r = 1 + \varepsilon$. Here, we fix $H(1 + \varepsilon, t)$ and $U(1 + \varepsilon, t)$ using (2.21). To commence computations, we then begin at a time $t = t_0 > 0$ for which the outer radius is at $R(t_0) = 1 + 2\varepsilon$, and $U(r, t_0)$ and $H(r, t_0)$ are again given by (2.21). The initial moment t_0 can be determined from (2.22), given a suitable choice for ε.

To advance solutions in time from this initial state, we first discretize in t. Then, at each time and given the current profile of $H(r, t)$, we solve the boundary-value problem (2.15)–(2.17) for $U(r, t)$ using Matlab's in-built solver bvp4c. With the computed velocity field $U(r, t)$ in hand, we next employ (2.14) and (2.18) to advance the thickness $H(r, t)$ and outer edge $R(t)$ to a new time, using a Lagrangian scheme. The time step is chosen sufficiently small that mass is conserved to less than 3 % over the duration of the computation.

Sample numerical solutions for axisymmetric spreading films are presented in figure 3. Panels (*a–d*) present series of snapshots of the film profile and $H(r, t)$ for Newtonian, power-law and Bingham fluids; corresponding time series of the outer radius $\overline{R}(t)$ are plotted in (*e*). The density ratios chosen for these solutions are similar to those for (*a*)

syrup spreading on oil ($\rho/\rho_b = 1.54/1.85 = 0.83$) and (*b*,*c*) Carbopol or Xanthan gum on oil ($\rho/\rho_b = 1/1.85 = 0.54$). The solutions mostly demonstrate a match with the expected early-time behaviour for $t \ll 1$, and are not evolved sufficiently far to observe an entrance to the long-time self-similar states for $t \gg 1$, catalogued in Ball & Balmforth (2021).

Note that the Bingham computation does not converge particularly closely to the early time solution in (2.21)–(2.22) for the value of $\varepsilon = 10^{-6}$ chosen (see panel (*d*)). It turns out that, for these parameter settings, and for most of the computations with finite Bi, it is a relatively poor approximation to neglect the yield stress in (2.16) for T_{rr}. If we instead keep this term, we recover an alternative approximation in which U satisfies

$$\frac{2(8\pi)^{1/n} n}{n+1} U^{\frac{n+1}{n}} {}_2F_1\left(\frac{n+1}{n}, \frac{1}{n}; \frac{2n+1}{n}; 8\pi BiU\right) = r - 1, \qquad (2.23)$$

where ${}_pF_q(a; b; c; z)$ is the generalized hypergeometric function of order $\{p, q\}$. The radius $\overline{R}(t)$ then follows from inverting (2.23) and using the kinematic condition in (2.17). As shown in figure 3(*d*,*e*), this alternative approximation is superior to the asymptotic solution in (2.21)–(2.22).

In the linear stability analysis below, we use values of $\varepsilon = 10^{-5} - 10^{-4}$ to commence the base state solution. This choice ensures that the inner boundary condition achieves a match to a solution with a diverging incoming depth that is otherwise independent of the precise choice for ε. Simultaneously, the choice ensures that radial gradients remain well resolved over the duration of the computation. Our inner boundary condition therefore avoids any need to match with a full Stokes-type solution at the edge of the pedestal, or impose a prescribed incoming flow depth H_0, as in Ball & Balmforth (2021), which would introduce arbitrary parameter that we cannot calibrate. Nevertheless, our boundary condition is equivalent to prescribing the incoming fluid depth, but then taking the limit $H_0 \gg 1$, leaving a solution that nearly diverges for $r \to 1$, but otherwise becomes independent of that parameter. Finally, having chosen ε, we compute the corresponding initial moment t_0 using (2.22) if $Bi = 0$. To avoid the relatively weak convergence to the small-time limit when $Bi > 0$, however, we instead use the alternative approximation in (2.23).

2.4. *Stability analysis*

To study non-axisymmetric perturbations to the axisymmetric base states, we set

$$h = H(r, t) + \hat{h}(r, t)e^{im\vartheta}, \quad u = U(r, t) + \hat{u}(r, t)e^{im\vartheta}, \qquad (2.24)$$

$$v = \hat{v}(r, t)e^{im\vartheta}, \quad R = \overline{R}(t) + \hat{R}(t)e^{im\vartheta}, \qquad (2.25)$$

where m is the angular wavenumber. The linear stability equations are the same as those in Ball & Balmforth (2021) (their equations (4.3)–(4.11)) and are restated in Appendix A. At the inner boundary $r = 1 + \varepsilon$, we further adopt the boundary conditions

$$\hat{u} = \hat{h} = \hat{v} = 0, \qquad (2.26)$$

assuming that the incoming flow cannot be perturbed. Finally, we use the initial conditions

$$\hat{R} = \hat{R}_0, \quad \hat{h} = \hat{u} = \hat{v} = 0, \quad \text{at } t = t_0. \qquad (2.27)$$

2.4.1. *Early times, $t \ll 1$*

At early times, the film forms a relatively narrow annulus where radial derivatives are amplified. Provided $m = O(1)$, we may then follow a very similar analysis to that presented

earlier, with the angular dependence not featuring to leading order. In view of the inner boundary and initial conditions, the perturbation to the radial velocity $\hat{u}$ remain small, and the dynamics becomes slaved to the motion of the outer edge. Considering the early time behaviour close to the pedestal, the perturbation to the outer radius then satisfies the leading-order kinematic condition (see Appendix (A11))

$$\hat{R}_t \sim U_r(\overline{R})\hat{R}. \tag{2.28}$$

Combining with $\overline{R}_t = U(\overline{R})$, we find

$$\hat{R}(t) \propto U(\overline{R}). \tag{2.29}$$

For $Bi \to 0$, we find

$$\hat{R}(t) = \hat{R}(t_0)\left[\frac{\overline{R}(t)-1}{\overline{R}(t_0)-1}\right]^{\frac{n}{n+1}} = \hat{R}(t_0)\left(\frac{t}{t_0}\right)^n. \tag{2.30}$$

Although the perturbation grows with time, it does not in comparison with the axisymmetric base state: here $\hat{R}/(\overline{R}-1) \propto t^{-1}$.

In this early-time limit, the effect of the fluid rheology is therefore felt only through the background velocity gradient, and $\hat{R}(t)$ increases fastest for Newtonian fluid ($n=1$). The growth of the perturbation corresponds to the geometrical spreading effect discussed by Sayag & Worster (2019b), which here factors in the thinning of the base state at the outer edge, as well as its stretching due to axisymmetric expansion. To see any sign of the Sayag & Worster instability (at order-one azimuthal wavenumbers), we must therefore proceed to later times.

2.4.2. *Later times, $t = O(1)$*

A numerical solution to the linear stability equations for Newtonian fluid ($n=1$, $Bi=0$) is shown in figure 4 for the mode with angular wavenumber $m=2$. The amplitude of the perturbation to the radius first grows linearly with time as predicted by (2.30), before slowing down to approach a scaling $t^{-0.8}$. This dependence is predicted by the analysis of long-time ($t \gg 1$) self-similar solutions to the problem provided in Ball & Balmforth (2021) (their Appendix A). Despite the different boundary conditions applying for $r \to 1$, this analysis applies here because, in the long time limit, the perturbations decay relatively quickly on proceeding inwards from the outer edge, eliminating any dependence on the conditions at the inner edge. The strengthening inward decay of the solutions can be observed in figure 4(b,c,d), and the final panel compares $\hat{u}$ and $\hat{v}$ with the corresponding self-similar solutions. Consequently, for $t \gg 1$, the linear modes are all still expected to decay relative to the expansion of the background axisymmetric state, regardless of the value of m, as explored in more detail by Ball & Balmforth (2021). Note that the solution, as with all those we present here, still lies a good way off the self-similar limit.

Low-angular-wavenumber solutions for a viscoplastic film ($n=0.4$, $Bi=1$) are shown in figure 5. Unlike the Newtonian case, the mode amplitudes now begin to grow relative to the base state at large times, as found in Ball & Balmforth (2021). For the modes shown, with $m=1-6$, growth begins when the base state has reached dimensional radii of almost $3\mathcal{L}$. Eventually, provided the solutions all reach the self-similar plastic plate explored in Ball & Balmforth (2021), the growth of the modes is expected to become exponential, with a rate that increases with m. For the experimentally relevant times plotted in figure 5 ($\overline{R}^2 - 1 < 10$), however, the modes have yet to reach this limit and are growing comparably
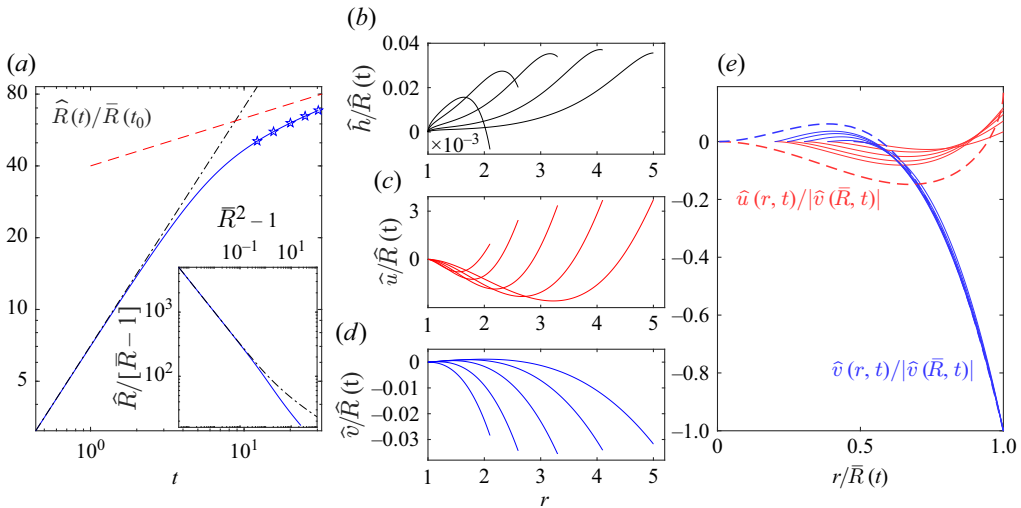
Figure 4. (*a*) Time series of the amplitude of the perturbation to the radius $\hat{R}$ scaled by its initial value, for a Newtonian film ($n = 1$, $Bi = 0$, $\varepsilon = 10^{-4}$) with angular wavenumber $m = 2$. The dot-dashed line shows the prediction in (2.30) and the dashed line indicates the long-time self-similar scaling (Ball & Balmforth 2021). In the inset, the amplitude is scaled by $\overline{R} - 1$, then plotted against $\overline{R}^2 - 1$. The spatial structure of the perturbations $(\hat{u}, \hat{v}, \hat{h})/\hat{R}$ is shown in (*b*,*c*,*d*) for the times indicated in (*a*). In (*e*) the velocity perturbations are scaled by $|\hat{v}(\overline{R}, t)|$ and plotted against $r/\overline{R}(t)$; the dashed lines show the similarity solution from Ball & Balmforth (2021).
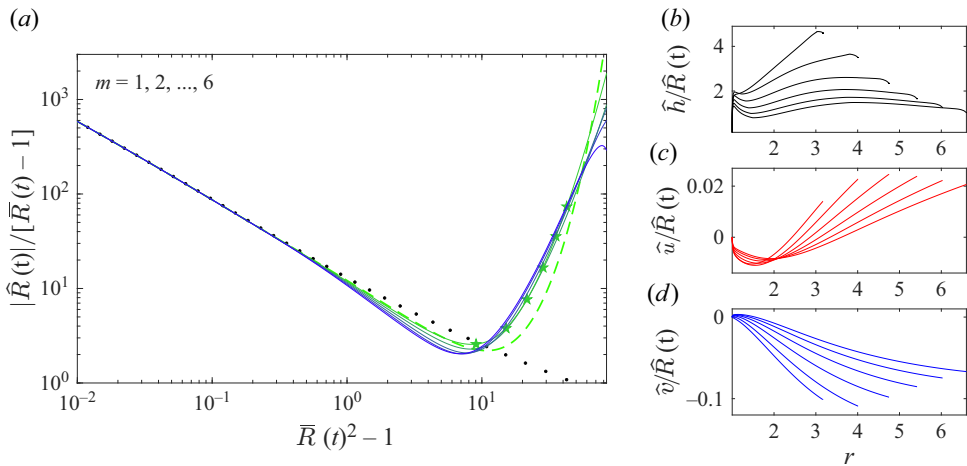

Figure 5. (*a*) Time series of $|\hat{R}|/[\overline{R} - 1]$ against $\overline{R}^2 - 1$ for a viscoplastic film ($n = 0.4$, $Bi = 1$, $\varepsilon = 10^{-4}/4$) with angular wavenumbers $m = 1, 2, \ldots, 6$ (from green to blue, with $m = 1$ shown dashed). The dotted black line shows the prediction in (2.30). Snapshots of scaled height and velocity perturbations $(\hat{h}, \hat{u}, \hat{v})/\hat{R}$ are shown in (*b*–*d*) for $m = 2$, at the times indicated by stars in (*a*).

to one another, except for the $m = 1$ mode which upturns more slowly. The spatial structure of the modes for $m = 2$ is relatively simple (figure 5(*b*,*c*,*d*)); more spatial oscillations appear at smaller radii with higher m (cf. Sayag & Worster (2019*b*); Ball & Balmforth (2021)).
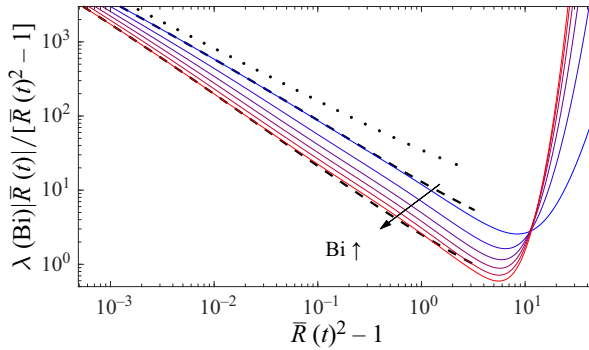
Figure 6. Time series of $\lambda(Bi)|\hat{R}|/[\overline{R}-1]$ against $\overline{R}^2-1$ for a viscoplastic film with varying $Bi = 1, 2, 3, 4, 5, 6$ (from blue to red), with $m=2$, $n=0.4$ and $\varepsilon = 10^{-4}/4$. The dashed black lines shows the prediction in (2.29) for $Bi=2$ and 6; the dotted black line shows the prediction in (2.30) for $Bi=0$.

The effect of increasing Bi whilst holding m and n fixed is illustrated in figure 6. For the small-time approximation in (2.23), the base state solution remains dependent on Bi. As a result, when the initial radius, $\overline{R}(t_0) = 1 + 2\varepsilon$, is translated to an initial time $t = t_0$ using (2.23), it implies that linear stability computations with different Bi are initiated at different times for a fixed ε. To flatten the landscape for an unbiased comparison, some scaling of the linear stability computations is therefore needed. In view of (2.29), we adopt the scaling factor

$$\lambda(Bi) = \frac{U(\overline{R}(t_0(Bi)))}{[U(\overline{R}(t_0(Bi)))]_{Bi=1}}, \tag{2.31}$$

which suppresses the differences in the perturbation $\hat{R}$ introduced by changing the time of initialization, and assures a common limit for $t \to 0$. In figure 6, we show radius perturbations scaled by $\lambda(Bi)$. At early times, the radius perturbation decays, with a rate that increases with yield stress. But for the largest times shown in the figure, the base state expands sooner towards the final, yield-stress-dominated, self-similar state for higher Bi (cf. figure 11 of Ball & Balmforth (2021)). As a consequence, the relatively strong instability in the self-similar state appears earlier. The two effects counter one another somewhat, leading to solutions that depend relatively mildly on Bingham number in figure 6. Indeed, for experimentally relevant times (corresponding to mean areas $\overline{R}^2 - 1 < 10$ or so), figure 6 suggests that instability is weak and largely independent of Bi.

Results for a power-law fluid film ($n = 0.12$ and $Bi = 0$) are shown in figure 7. As in the Newtonian case, the modes initially grow as expected by (2.30), decaying relative to the base state flow. The spatial structure of the modes is similar to that seen for the viscoplastic film in figure 5. At early times, modes with higher-wavenumber decay slightly faster, a trend that eventually reverses. The most conspicuous feature seen in figure 7(*a*) is the onset of oscillatory growth for $m > 1$ at the final times, a feature noted previously in Ball & Balmforth (2021). This leads to a node in the mode amplitude $|\hat{R}|$, visible as the sharp negative spike in the logarithmic plot in figure 7(*a*). The non-zero frequency suggests that patterns form pulsating standing waves or rotate in angle in the manner of a travelling wave, depending on initial conditions. Oscillatory growth also arises for finite Bi; the solutions for larger values of m in figure 5(*a*) are on the brink of such behaviour,
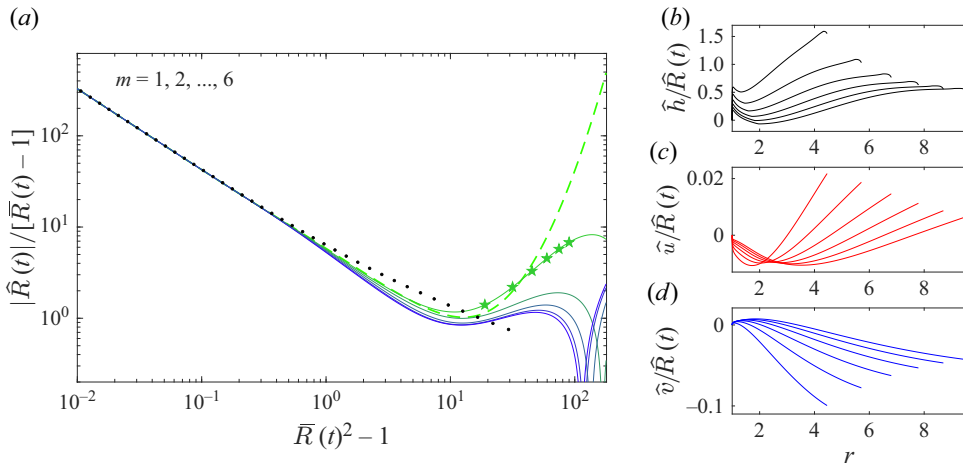
Figure 7. (*a*) Time series of $|\hat{R}|/[\overline{R} - 1]$ against $\overline{R}^2 - 1$ for a power-law film ($n = 0.12$, $Bi = 0$, $\varepsilon = 10^{-4}/4$) with angular wavenumbers $m = 1, 2, \ldots, 6$ (from green to blue, with $m = 1$ shown dashed). The dotted black line shows the prediction in (2.30). Snapshots of scaled height and velocity perturbations $(\hat{h}, \hat{u}, \hat{v})/\hat{R}$ are shown in (*b*–*d*) for $m = 2$, at the times indicated in (*a*).

which accounts for the downturn in the amplitude for the mode with highest m at the right end of the plot.

3. Experiments

3.1. *Set-up*

To complement theory, we conducted a series of experiments in which a complex fluid was floated out on top of a bath of denser viscous fluid, as illustrated in figure 2. For the complex fluid we used aqueous suspensions of either Carbopol, with concentration 0.2 % (Ultrez 21, neutralized with sodium hydroxide), or Xanthan gum, with concentration 0.6 %. Fits to the flow curves of these fluids, as measured in a Kinexus Malvern rheometer (employing roughened parallel plates and a controlled decreasing shear-rate ramp) are shown in figure 8. Parameter values and relevant dimensionless groups are presented in table 1. Note that the fastest radial speeds in the experiments are of order a few millimetres per second, over radial scales of a few centimetres, implying strain rates of 0.1 s^{-1} or less. Viscoelastic relaxation times for Carbopol and Xanthan gum are commonly quoted to be a second or less. Therefore, Weissenberg numbers are expected to be relatively small, suggesting that fluid viscoelasticity is not relevant.

The bath was filled up to the top with a perfluoropolyether oil (Galden HT 270, Lesker Cor.). A pedestal with a height equal to the depth of the bath $\mathcal{H}_b$ was placed in the centre of the bath to act as a launch stage for the complex fluid, which was emplaced from a tube connected to a syringe pump delivering constant flux Q. Once the film of complex fluid spread out over the bath, any displaced oil flowed over the brim to help maintain the level of the bath. Images taken of the film from below were processed to extract the outer edge (see figure 9). A second camera positioned at the level of the bath was used to record side images of the floating film and to look for any changes in the depth of the surrounding oil. No such changes in depth were observed, and capillary effects along the outer brim of the bath did not appear to be significant.
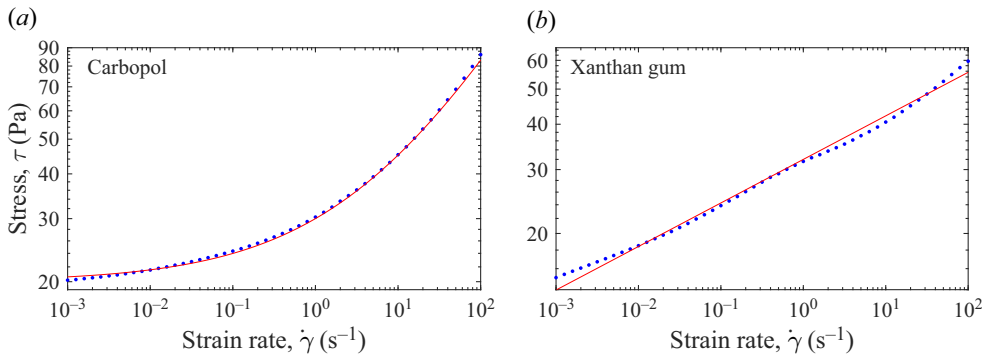
Figure 8. Flow curves for the two complex fluids used in the experiments. In these decreasing shear-rate ramps, there are ten samples per decade of shear rate, and a 60 s wait time at each $\dot{\gamma}$ to reach steady state. The points show the rheometer measurements, the lines indicate the fits in table 1.
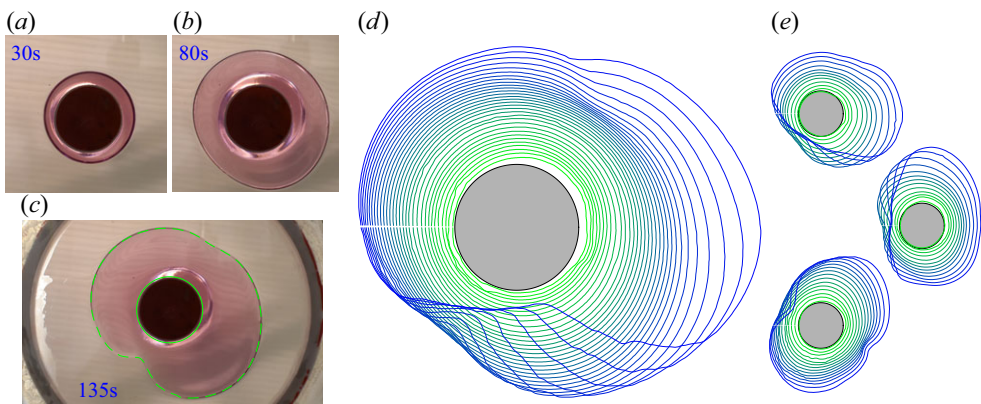

Figure 9. (*a*)–(*c*) Photographs from below and (*d*) extracted outlines of the fluid edge for an experiment with Carbopol pumped above an oil bath of depth 10.5 mm with flux 20 ml/min. The reconstruction of the edge outline from the photograph is also indicated in (*c*) as a green dashed line, as is the outer edge of the pedestal (green solid line). Three other tests for the same experimental conditions are shown in (*e*). In (*d*), the outlines are 5 s apart; in (*e*), the interval is 10 s. These outlines are coloured by time, from green to blue. The pedestal (shown in black in (*a*–*c*) and shaded grey in (*d*,*e*)) has a radius of 1.7 cm.

3.2. *First observations*

The observed phenomenology of experiments with Carbopol is illustrated in figure 9, which presents three successive images (taken from above) of the expanding floating film in one of the experiments. Also displayed are reconstructed outlines of the outer edge for this particular test, and for three other repetitions of it. After pumping commenced, the fluid deposited on the pedestal spreads out, eventually reaching the edge of the pedestal and coming into contact with the oil. The film then floated out above the bath, initially in a roughly axisymmetrical manner, modulo any imperfections associated with a non-axisymmetric contact with the oil at the edge of the pedestal (figure 9*a*,*b*). At later times, however, the film significantly lost axisymmetry as one or two 'clefts' appeared at the outer edge (figure 9*c*). These defects grew, diverting fluid sideways, with their roots retreating backwards and often rotating around the pedestal (figure 9*d*). As illustrated in figure 10, this phenomenology spanned the entire range of experiments with Carbopol performed with varying flux.
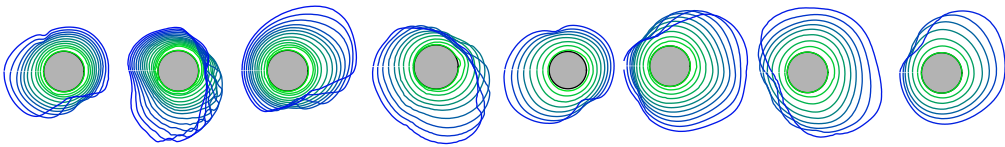
Figure 10. Outlines of the fluid edge for experiments with Carbopol (from above, coloured by time, from green to blue) for tests with increasing flux (proceeding from left to right with $Q = 1.25, 2.5, 5, 10, 40, 60, 80, 120$ ml/min). The intervals between these outlines varies between experiment.
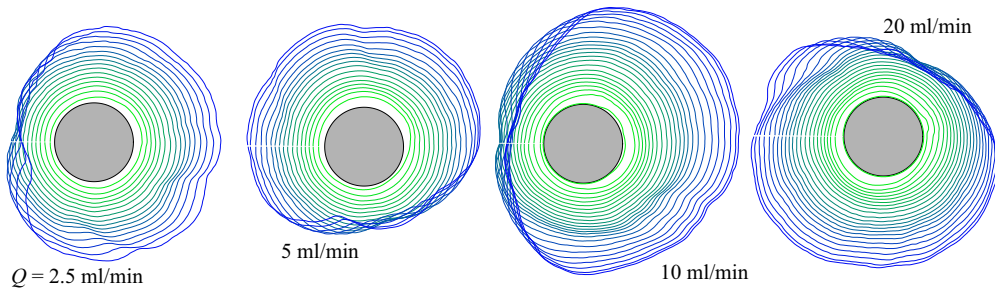

Figure 11. Outlines of the fluid edge for experiments with Xanthan gum for the fluxes indicated. The outlines are 10 s apart and coloured by time, from green to blue.
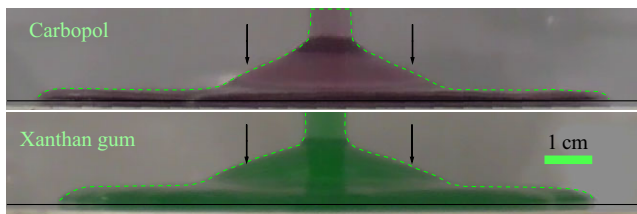

Figure 12. Side images of floating films of Carbopol and Xanthan gum, showing the profiles above the rim of the bath. The arrows indicate the edges of the pedestal with radius $\mathcal{L} = 1.7$ cm, as apparent from images taken before the arrival of the complex fluid.

In repetitions of the tests with the same experimental parameter settings, the clefts appeared at differing angular positions (see figure 9e). Similarly, in figure 10 the clefts have no preferred angular orientation. Thus, there appear to be no angular bias in the tests due to an imperfect experimental set-up. That said, however, the angular position at which a cleft formed did, on occasion, appear to be correlated with the location where the complex fluid film first flowed out from the pedestal, as can be seen by careful inspection of the early contours in figures 9 and 11.

The dynamics was similar in tests with Xanthan gum, as illustrated in figure 11. For this material, however, the clefts responsible for prompting non-axisymmetric patterns were much more rounded and developed after a longer time. The degree of asymmetry in the final patterns was also less pronounced.

Images taken from the side of the experiment for films of both Carbopol and Xanthan gum are illustrated in figure 12. The thinning of the film as it descends off the pedestal is clear, as is the much flatter floating film that then forms (cf. figure 3). At the outer edge of the film, the fluids are visibly rounded off, and probably thickened, by surface tension. Such features, coupled with the perspective of the camera, make thicknesses hard to estimate. Nevertheless, both images suggest that the film is several millimetres
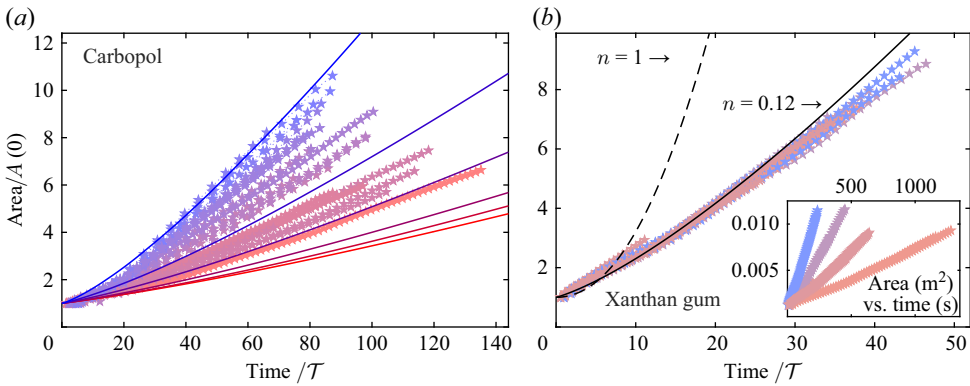
Figure 13. Plots of the area of the footprint of the film, as observed from above and scaled by the area of the pedestal for tests with (*a*) Carbopol and (*b*) Xanthan gum. The stars indicate suites of experiments with varying flux (colour from red to blue indicating increasing Q), the lines show theoretical results for $n = 0.4$ and $Bi = 1, 2, \ldots, 6$ in (*a*), and $n = 0.12$ (solid), and $n = 1$ (dashed) in (*b*) (plus $Bi = 0$). The inset in (*b*) shows the unscaled data; the fluxes are $Q = 2.5, 5, 10$ and 20 ml/min. For (*a*), $Q = 1.25, 2.5, 5, 10, 20, 40, 60, 80, 120$ and 160 ml/min.

thick, given that submergences of a factor of two or so are expected from the density differences. Such depths are larger than our estimates for the characteristic height scale $\mathcal{H}$ in the theoretical model, as quoted in table 1. That said, the dimensionless film depths achieved in model solutions suggest that actual depths can be larger than $\mathcal{H}$ by factors of order unity (see figure 3). More awkward is the rounding of the film profile at the outer edge, which suggests a prominent effect of surface tension. Indeed, we estimate capillary lengths to be between $1 - 3$ mm (see table 1). We discuss this issue further in § 4.

3.3. *Analysis*

If there is no yield stress, our dimensional analysis in § 2.1 indicates that we arrive at an axisymmetric problem that is free of any parameters, but for the power-law exponent n, when horizontal length are scaled by the radius of the pedestal $\mathcal{L}$ and time by the scale $\mathcal{T}$ defined in (2.2). Thus, with this scaling of lengths and time, data for axisymmetric films of Xanthan gum with different fluxes should collapse. Conversely, corresponding Carbopol data should remain dependent on the dimensionless yield-stress parameter, the Bingham number Bi in (2.3).

Although the experimental films do not remain axisymmetrical, we follow in this vein and seek to collapse the experimental data by plotting the scaled area of the films footprint above the bath, $A(t)/A(0)$, against $t = \tilde{t}/\mathcal{T}$ ($\tilde{t}$ being dimensional time). The area $A(t)$ is calculated from integrating the outlines of the fluid edge obtained from image analysis, as shown in figures 9, 10 and 11. We take $A(0)$ to be the area of the pedestal as seen in the outlines, and $t = 0$ to be the time of the last image before we observe the fluid to fall off the pedestal.

Figure 13 presents the results for suites of experiments with both Carbopol and Xanthan gum. Also included are plots of $\pi \overline{R}^2$ for axisymmetric solutions to the thin-film model for $(n, Bi) = (0.12, 0)$ (for comparison with Xanthan gum data), and varying Bingham number with $n = 0.4$ (to compare with Carbopol; see table 1).

The scaling of the Xanthan gum tests convincingly collapses the data. For Carbopol, there is a noticable difference at higher values of the Bingham number. This may arise
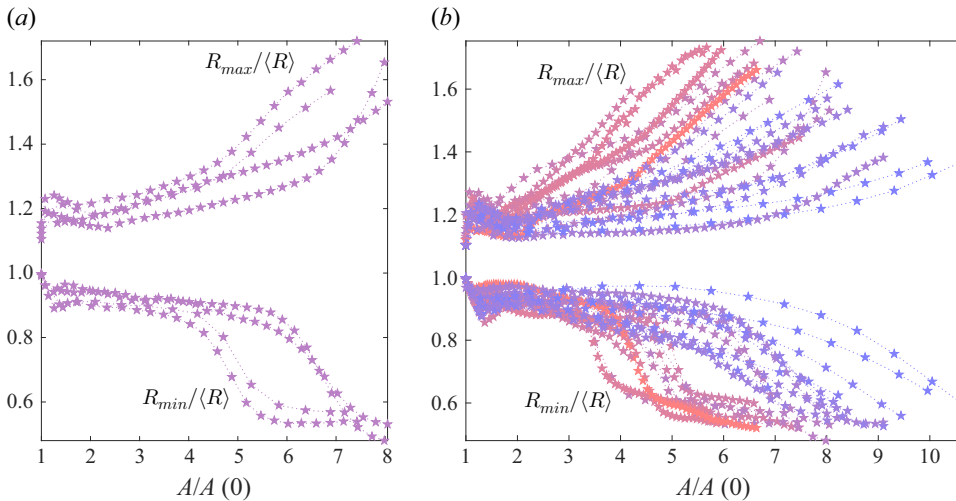
Figure 14. (*a*) Times series of the minimum and maximum, $R_{min}(t)$ and $R_{max}(t)$, of the radius $R(\theta, t)$ over angle plotted against scaled area, for four Carbopol experiments at flux $Q = 20$ ml/min. The angular variation and extrema are normalized by the mean radius $\langle R \rangle(t)$. In (*b*) data for the full suite of Carbopol tests with varying flux (coloured by Q increasing from red to blue) are shown.

because the experimental films are not that shallow, especially above the pedestal, and fluid may be piling up there. Qualitatively at least, the trend with Bi is reproduced by the model.

More quantitative details of the development of non-axisymmetry are shown in figure 14. In (*a*), the four tests with Carbopol and flux $Q = 20$ ml/min from figure 9 are plotted, showing the angular maximum and minimum. Each are scaled with the mean radius, $\langle R \rangle(t)$ to remove the effect of film expansion. As can be seen from this figure, the onset of non-axisymmetry, or equivalently the appearance of a cleft along the outer edge, can be observed as an abrupt decrease in $R_{min}/\langle R \rangle$. However, the moment at which this happens varies significantly between the tests, which probably arises from non-axisymmetric perturbations when the film first detaches from the pedestal, which are difficult to control. In figure 14(*b*), we plot the entire suite of tests with Carbopol and varying flux. There is a clear trend with Q revealed by the plot: films with smaller fluxes (higher Bi) become non-axisymmetric for smaller scaled areas. This correlation with flux can also be seen through careful inspection of the outlines in figure 11.

Corresponding results for Xanthan gum are shown in figure 15. Again, there is some suggestion that the development of the clefts and non-axisymmetry occur later for higher fluxes. This is inconsistent with the theoretical model, where the only non-dimensional parameter is the power-law exponent, implying that the data for different fluxes should collapse (as for the average radius in figure 13). One possible explanation for this discrepancy is that the Xanthan gum has a small yield stress. Indeed, yield stresses of $O(1)$Pa are not ruled out by the rheometry in figure 8. However, such yield stresses imply Bingham numbers of $O(10^{-1})$, which are relatively small. Alternatively, the residual dependence on flux may result from the manner in which non-axisymmetric instability is initialized when the Xanthan gum descends off the pedestal, which we cannot control. This initialization creates an initial perturbation shown by the difference between R_{min} and R_{max} at $t = 0$ in figure 15 (and figure 14 for Carbopol). Despite this, those perturbations appear to largely subside before instability truly sets in at later times.
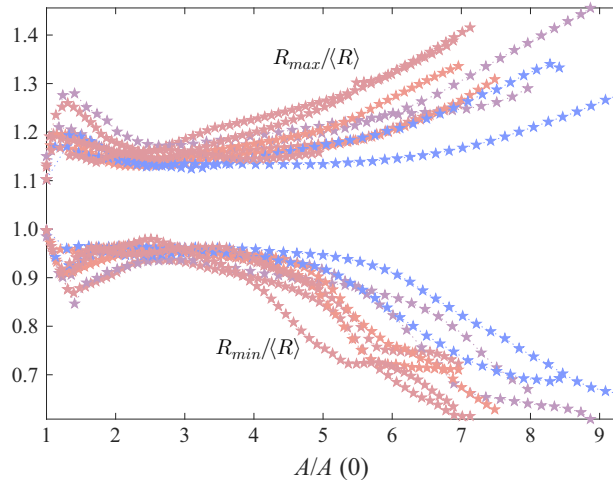
Figure 15. Times series of minimum and maximum, $R_{min}(t)$ and $R_{max}(t)$, of the radius $R(\theta, t)$ over angle plotted against scaled area, for Xanthan gum experiments with varying flux (coloured by Q increasing from red to blue). The angular variation and extrema are normalized by the mean radius $\langle R \rangle(t)$.

4. Discussion

The linear instability of Sayag & Worster reported for expanding cylinders of power-law fluid is modified in the geometry of a thinning expanding film, with shear thinning no longer driving a loss of axisymmetry at early times (when the degree of expansion is small). Instead, at later times, when the film has expanded in radius by a factor of two or so, shear-thinning hoop stresses do come into play to drive non-axisymmetric instabilities. We have presented theoretical results to illustrate these features, and compared them with laboratory experiments. The experiments confirm that non-axisymmetric patterns begin to grow when the dimensionless area of the film is $O(1)$. In both the theoretical model and experiments, unstable modes possess relatively low angular wavenumber, and the loss of symmetry is not particularly dramatic.

The experimental patterns first appear when small indentations or clefts form at a few angular locations around the outer edge. The roots of these defects then retreat to smaller radii, often rotating sideways in angle. The possibility that patterns can rotate in angle also arises in the theory: perturbations develop finite angular phase speeds at later times, indicating the onset of travelling waves.

When the oil in the bath is replaced by salty water, the experiments are completely different, with dramatic non-axisymmetric patterns appearing relatively quickly. Following Ball *et al.* (2022), we believe these patterns have an origin that is different to Sayag & Worster's instability: the expanding film appears to fracture under extensional stresses at the fluid edge, which may be facilitated by a reduction in fracture toughness in the presence of water (the film's solvent). Indeed, the present theory and experiments suggest that Sayag & Worster's instability for a floating film does not appear at early times and does not lead to such a dramatic loss of axisymmetry.

There are some notable discrepancies between the predictions of the thin-film model and the experimental observations: although the average expansion of the film is fairly well reproduced, the manner in which the strength of the non-axisymmetric patterns depends on flux is not. For Carbopol, the significant enhancement in pattern strength at lower flux implies that instability should become stronger for higher Bingham number. The theory, however, predicts a much weaker dependence, at least for the times corresponding to

the duration of the experiments. Similarly, with Xanthan gum, the patterns are predicted theoretically to be independent of flux for a given pumped area; the experiments, however, still display some flux dependence. Both discrepancies may result from the way in which non-axisymmetric patterns are initialized. In the experiments, this initialization occurs when the film falls abruptly off the pedestal, which is relatively uncontrolled and difficult to repeat, creating asymmetries in both the position of the outer edge and thickness distribution.

Another limitation of the thin-film model is that neither surface nor interfacial tensions are included. As a result, our axisymmetric base states feature an unphysical vertical cliff at their edges. By contrast, the films in the experiments are noticeably rounded off along their upper surfaces with air (visualizing the lower interface with oil was more challenging). Estimates of the capillary length for the experiments are consistent with the scale at which this rounding takes place. It is not obvious what impact this rounding has on the linear stability analysis. Curvatures in the angular direction are expected to dampen any non-axisymmetric fingering instability. However, for the thin film, the dominant curvature is perpendicular, in the (r, z) plane. In Hele-Shaw cells, in which thicknesses are fixed, such curvatures can play a relatively minor role, contributing primarily a constant capillary pressure. For our films, however, the thickness evolves, changes the local curvature at the edge. In our view, the neglect of surface tension is therefore the most problematic omission in the theoretical model.

Author contributions. All author's contributed equally to the development of the theoretical model, carrying out the laboratory experiments, and preparing the manuscript.

Data availability statement. For all of the experiments, the mean, minimum and maximum radius against time are plotted in the figures 13, 14 and 15. For all except a subset of repeats, the edge outline is plotted as a function of time in figures 9, 11 and 10. Any further data, including raw images taken, will be made available upon request.

Appendix A. Linear stability equations

To study non-axisymmetric perturbations to the axisymmetric base states, we set

$$h = H(r, t) + \hat{h}(r, t)e^{im\vartheta}, \quad u = U(r, t) + \hat{u}(r, t)e^{im\vartheta}, \tag{A1}$$

$$v = \hat{v}(r, t)e^{im\vartheta}, \quad R = \overline{R}(t) + \hat{R}(t)e^{im\vartheta}, \tag{A2}$$

where m is the angular wavenumber.

Linearizing the force balance and continuity equations (2.6)–(2.5), we find the amplitudes $\{\hat{h}, \hat{u}, \hat{v}, \hat{R}\}$ satisfy

$$0 = \left[H(\hat{h} - 2\hat{\tau}_{rr} - \hat{\tau}_{\theta\theta}) - \hat{h}(2T_{rr} + T_{\theta\theta}) \right]_r - \frac{im}{r} H\hat{\tau}_{r\theta} + \frac{H}{r}\left(\hat{\tau}_{\theta\theta} - \hat{\tau}_{rr}\right) + \frac{\hat{h}}{r}\left(T_{\theta\theta} - T_{rr}\right), \tag{A3}$$

$$0 = \frac{1}{r}\left(r^2 H\hat{\tau}_{r\theta}\right)_r - im\left[H(\hat{h} - 2\hat{\tau}_{\theta\theta} - \hat{\tau}_{rr}) - \hat{h}(2T_{\theta\theta} + T_{rr}) \right], \tag{A4}$$

$$\hat{h}_t + \frac{1}{r}[r(U\hat{h} + H\hat{u})]_r + \frac{im}{r}H\hat{v} = 0, \tag{A5}$$

where the perturbations to the stress components are given by

$$\hat{\tau}_{rr} = \alpha_{rr}\hat{u}_r + \frac{1}{r}\beta_{rr}(\hat{u} + im\hat{v}), \qquad \hat{\tau}_{\theta\theta} = \alpha_{\theta\theta}\hat{u}_r + \frac{1}{r}\beta_{\theta\theta}(\hat{u} + im\hat{v}), \tag{A6}$$

$$\hat{\tau}_{r\theta} = \mu\left[r\frac{\partial}{\partial r}\left(\frac{\hat{v}}{r}\right) + \frac{im}{r}\hat{u}\right], \tag{A7}$$

with

$$\alpha_{rr} = 2\left[\mu + 4\mu' U_r\left(2U_r + \frac{1}{r}U\right)\right], \qquad \beta_{rr} = 8\mu' U_r\left(\frac{2}{r}U + U_r\right), \tag{A8}$$

$$\alpha_{\theta\theta} = \frac{8}{r}\mu' U\left(2U_r + \frac{1}{r}U\right), \qquad \beta_{\theta\theta} = 2\left[\mu + \frac{4}{r}\mu' U\left(\frac{2}{r}U + U_r\right)\right], \tag{A9}$$

$$\mu = \frac{1}{\dot{\Gamma}}(Bi + \dot{\Gamma}^n), \qquad \mu' = -\frac{1}{2\dot{\Gamma}^3}[Bi + (1-n)\dot{\Gamma}^n]. \tag{A10}$$

The outer boundary conditions, after a Taylor expansion about the unperturbed edge, are

$$\left.\begin{array}{r}\hat{R}_t = U_r\hat{R} + \hat{u} \\ H\left(\hat{h} - 2\hat{\tau}_{rr} - \hat{\tau}_{\theta\theta}\right) - \hat{h}\left(2T_{rr} + T_{\theta\theta}\right) + \left[\frac{1}{2}H^2 - H(2T_{rr} + T_{\theta\theta})\right]_r \hat{R} = 0 \\ \hat{\tau}_{r\theta} - im\hat{R}(T_{\theta\theta} - T_{rr})/\overline{R} = 0\end{array}\right\} \quad \text{at } r = \overline{R}. \tag{A11}$$

These equations can be solved numerically as an initial-value problem. Starting with the initial conditions described in § 2.4, we discretize in t. At each time step, given the current profile of $\hat{h}(r, t)$, we solve the boundary-value problem (A3)–(A4) for $\hat{u}(r, t)$ and $\hat{v}(r, t)$ using Matlab's in-built solver bvp4c. A Lagrangian scheme is then used to advance the thickness $\hat{h}(r, t)$ solving (A5), and hence calculate the radial perturbation $\hat{R}$. This is the same numerical scheme used to solve the initial-value problem in Ball & Balmforth (2021).

REFERENCES

BALL, T.V. & BALMFORTH, N.J. 2021 Instability of sliding viscoplastic films. *J. Fluid Mech.* **912**, A23.

BALL, T.V., BALMFORTH, N.J. & DUFRESNE, A.P. 2021 Viscoplastic fingers and fractures in a hele-shaw cell. *J. Non-Newtonian Fluid Mech.* **289**, 104492.

BALL, T.V., BALMFORTH, N.J., MORRIS, S.W. & DUFRESNE, A.P. 2022 Fracture patterns in viscoplastic gravity currents. *J. Fluid Mech.* **934**, A31.

BALMFORTH, N.J. 2018 Viscoplastic asymptotics and other analytical methods. In *Viscoplastic Fluids: From Theory to Application, CISM*. Springer.

BALMFORTH, N.J., FRIGAARD, I. & OVARLEZ, G. 2014 Yielding to stress: recent developments in viscoplastic fluid mechanics. *Ann. Rev. Fluid Mech.* **46** (1), 121–146.

CRASTER, R.V. & MATAR, O.K. 2009 Dynamics and stability of thin liquid films. *Rev. Mod. Phys.* **81** (3), 1131–1198.

DI PIETRO, N. & COX, R. 1979 The spreading of a very viscous liquid on a quiescent water surface. *Q. J. Mech. Appl. Math.* **32** (4), 355–381.

ENGLAND, P. & MCKENZIE, D. 1982 A thin viscous sheet model for continental deformation. *Geophys. J. Intl* **70** (2), 295–321.

ENGLAND, P. & MCKENZIE, D. 1983 Correction to: a thin viscous sheet model for continental deformation. *Geophys. J. Intl* **73** (2), 523–532.

HUTCHINSON, A. J. & WORSTER, M. 2024 Fracturing behaviour of a shear-thinning fluid in a lubricated hele-shaw cell. *J. Fluid Mech.* **1003**, A6.

KOCH, D.M. & KOCH, D.L. 1995 Numerical and theoretical solutions for a drop spreading below a free fluid surface. *J. Fluid Mech.* **287**, 251–278.

MACAYEAL, D.R. 1989 Large-scale ice flow over a viscous basal sediment: theory and application to ice stream b, antarctica. *J. Geophys. Res.: Solid Earth* **94** (B4), 4071–4087.

MACAYEAL, D.R. & BARCILON, V. 1988 Ice-shelf response to ice-stream discharge fluctuations: i. unconfined ice tongues. *J. Glaciol.* **34** (116), 121–127.

ORON, A., DAVIS, S. H. & BANKOFF, S. 1997 Long-scale evolution of thin liquid films. *Rev. Mod. Phys.* **69** (3), 931–980.

PEGLER, S. S. & WORSTER, M. 2012 Dynamics of a viscous layer flowing radially over an inviscid ocean. *J. Fluid Mech.* **696**, 152–174.

SAYAG, R. & WORSTER, M. 2019*a* Instability of radially spreading extensional flows. Part 1: experimental *a*nalysis. *J. Fluid Mech.* **881**, 722–738.

SAYAG, R. & WORSTER, M. 2019*b* Instability of radially spreading extensional flows. Part 2: theoretical analysis. *J. Fluid Mech.* **881**, 739–771.

SCHOOF, C. 2007 Marine ice-sheet dynamics. part 1. the case of rapid sliding. *J. Fluid Mech.* **573**, 27–55.

SCHOOF, C. 2011 Marine ice sheet dynamics. part 2. a stokes flow contact problem. *J. Fluid Mech.* **679**, 122–155.

SCHOOF, C. & HEWITT, I. 2013 Ice-sheet dynamics. *Annu. Rev. Fluid Mech.* **45** (1), 217–239.